npj | climate and atmospheric science

Article

Published in partnership with CECCR at King Abdulaziz University

https://doi.org/10.1038/s41612-026-01393-w

Sea surface height variability shapes Siberian Arctic Ocean circulation and Pacific Water inflow

Check for updates

Taewook Park[1] ✉, Kyoung-Ho Cho[1], Eunho Lee[1], Igor V. Polyakov[2] & Eun Jin Yang[1]

The Siberian Arctic Ocean links river runoff, sea ice, and Pacific–Atlantic exchanges, yet the drivers of its circulation variability remain poorly constrained. Using multi-decadal satellite altimetry, ocean reanalysis products, and in situ observations with cyclostationary empirical orthogonal function analysis, we show that shelf and slope currents are governed by distinct mechanisms across timescales. Seasonally, the Eastern Siberian Shelf Current is primarily regulated by salinity-driven sea-surface-height (SSH) gradients, with winds secondary, whereas the narrow Siberian Coastal Current is buoyancy-driven and strongly enhanced by summer winds. Interannually, the Siberian Slope Current captures a recent atmospheric transition from the Arctic Oscillation to the Arctic Dipole. We further identify a Siberia–Alaska sea-level-pressure dipole that modulates SSH gradients and regulates Pacific Water inflow through the Bering Strait, providing a physically based inflow index. Overall, SSH integrates buoyancy forcing, wind-driven circulation, and basin-scale atmospheric variability, identifying the Siberian Arctic Ocean as a key region for Arctic Ocean circulation and climate variability.

Arctic warming is occurring at nearly four times the rate of the global average[1], causing profound changes in its sea ice, ocean circulation, and Arctic ecosystems[2–5]. The extent and thickness of Arctic sea ice have declined substantially[6,7], and projections suggest that the region may lose all summer sea ice cover within decades, even under reduced emissions scenarios[8]. The Arctic Ocean plays a central role in climate variability, with circulation features such as the Beaufort Gyre, the transpolar drift, and Siberian coastal currents actively redistributing heat and freshwater[9–13]. The East Siberian continental shelf plays a particularly important role in this variability because of the convergence between river discharge, sea-ice processes, and Pacific Water inflow, thereby shaping stratification, vertical mixing, and biogeochemical cycling[14,15]. Additionally, ocean circulation variations in this region have been linked to anomalous biogeochemical events and enhanced shelf–basin interactions under rapid warming[16,17], underscoring the need to understand the dynamics of the Eastern Siberian Shelf Current (ESSC) and its associated climatic impacts. Atlantic inflows are increasingly recognized as key drivers of sea-ice decline and circulation shifts in the Eurasian Basin[18,19], reinforcing the need to investigate shelf–basin linkages in the Arctic Ocean under rapid climate change.

Gateway exchange further modulates the variability of these processes. The Bering Strait provides the sole Pacific inflow to the Arctic Ocean, with seasonal and interannual transport variations arising in response to atmospheric forcing, such as local winds and basin-scale atmospheric conditions[20–23]. Bering Strait transport influences stratification and biogeochemical responses in the Arctic Ocean, and recent studies have further resolved Pacific inflow pathways across the Chukchi Shelf[24]. Given the critical role of Bering Strait transport in shaping future changes in Arctic Ocean circulation, identifying robust modes that capture its variability is essential for advancing understanding and improving prediction of Pacific Water inflow.

Sea surface height (SSH) offers an integrated perspective on Arctic Ocean circulation by capturing both basin- and shelf-scale processes under ice cover[25]. Satellite altimetry and reanalysis data have revealed features such as the freshwater dome in the Beaufort Gyre[26–28] and have highlighted key circulation drivers, including sea-ice melt, river runoff[29,30], Pacific Water inflow[20], and wind-driven Ekman convergence[31]. Salinity-driven density gradients further shape cross-shelf SSH slopes, strongly influencing buoyancy-driven currents[14,32,33], suggesting that the variability in Arctic Ocean circulation arises from the interplay between multiple forcing factors.

Large-scale atmospheric modes also play a critical role in governing Arctic Ocean circulation. The Arctic Oscillation (AO), which dominates winter sea-level pressure variability[34], and the Arctic Dipole (AD), which is characterised by a meridional pressure gradient between the Atlantic and Pacific sectors[35,36], both strongly influence this circulation. The AO and AD wind anomalies drive distinct cyclonic and anticyclonic SSH responses[37–39]. However, the AO–SSH relationship weakened after the mid-1990s[28,40], and a

---

[1]Division of Ocean and Atmosphere Sciences, Korea Polar Research Institute, Incheon, Republic of Korea. [2]International Arctic Research Center and College of Natural Science and Mathematics, University of Alaska Fairbanks, Fairbanks, AK, USA. ✉e-mail: twpark@kopri.re.kr

recent study has suggested an increasing AD influence[41]. This shift underscores the need to clarify how atmospheric regime changes are expressed in SSH variability across spatial and temporal scales.

In this study, we analysed multi-decadal SSH variability from satellite altimetry and ocean reanalysis data using a cyclostationary empirical orthogonal function (CSEOF), allowing for seasonal cycles to be incorporated into the EOF framework[42,43]. This approach enabled us to resolve the dynamics of the Siberian shelf-slope currents and to investigate Arctic gateway connectivity, with a particular focus on the Bering Strait. These results provide an integrated framework for understanding the circulation system of the Siberian Arctic Ocean.

Results and discussion

Seasonal dynamics of the Eastern Siberian Shelf Current

We investigated SSH variability by applying the CSEOF technique to satellite altimetry-derived dynamic ocean topography (DOT) for 2003–2020 and to ORAS5 reanalysis data for 1979–2018 (Methods). The leading CSEOF mode highlights a pronounced seasonal cycle over the East Siberian Shelf region (Fig. 1a, c). Sea surface height peaks during September–November and reached a minimum during March–May, with satellite DOT and ORAS5 showing strong agreement between their respective principal components ($r = 0.92$; Fig. 1e). The multi-year monthly SSH anomalies and the seasonal climatology (Figs. S1 and 2e–h) confirm that coastal SSH is elevated relative to offshore areas during summer and autumn, thereby steepening the cross-shelf slope and sustaining an eastward ESSC. In situ observations from the MB9 mooring station[19] further support this seasonal variability (Fig. S2). Currents flow eastward in summer, consistent with a strong salinity gradient, and flow westward in winter, when the gradient weakens and reverses. ORAS5 reproduces this seasonal reversal in both timing and direction, albeit with reduced magnitudes owing to temporal averaging, confirming that this reanalysis dataset captures the essential dynamics of the shelf current. Cross-shelf transects averaged over 73°–75°N provide a clear spatial representation of this process. As the halocline strengthens in summer, coastal SSH rises relative to offshore waters, thereby reinforcing the geostrophic current. During winter, the

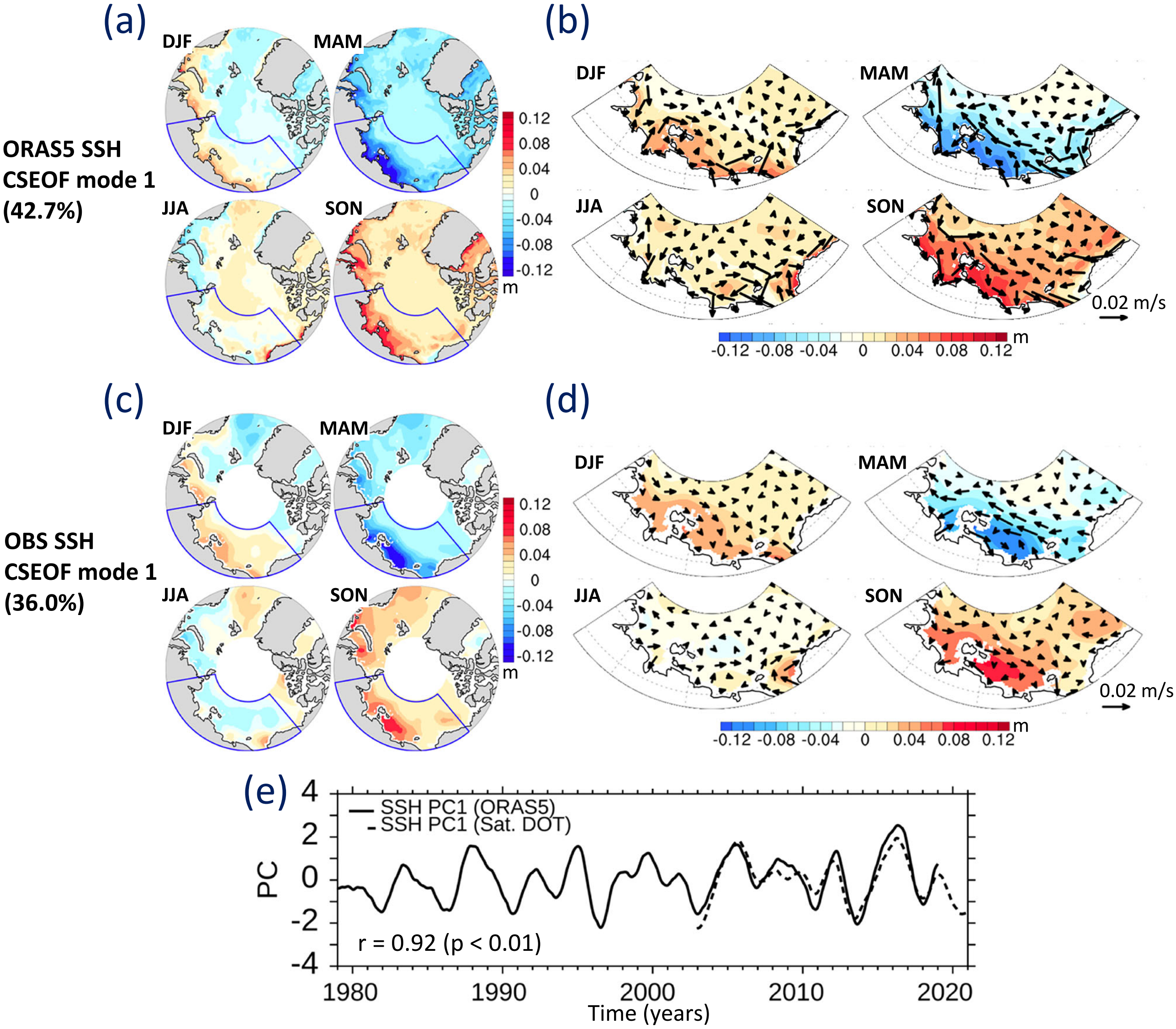

Fig. 1 | Dominant seasonal SSH mode (Mode 1). a, **b** Spatial patterns of SSH anomalies (shading; m) and the associated geostrophic currents (vectors) for the leading cyclostationary EOF (CSEOF) mode derived from ORAS5 reanalysis, shown for boreal winter (DJF), spring (MAM), summer (JJA), and autumn (SON). **c**, **d** Corresponding SSH anomaly and geostrophic current patterns obtained from satellite-derived dynamic ocean topography (DOT). The blue outline in (**a**, **c**) indicates the region displayed in the enlarged maps with overlaid current vectors in (**b**, **d**). **e** Principal component (PC) time series of the dominant seasonal mode derived from ORAS5 (solid line) and satellite DOT (dashed line), demonstrating strong agreement between the model output and observations ($r = 0.92$, $p < 0.01$).

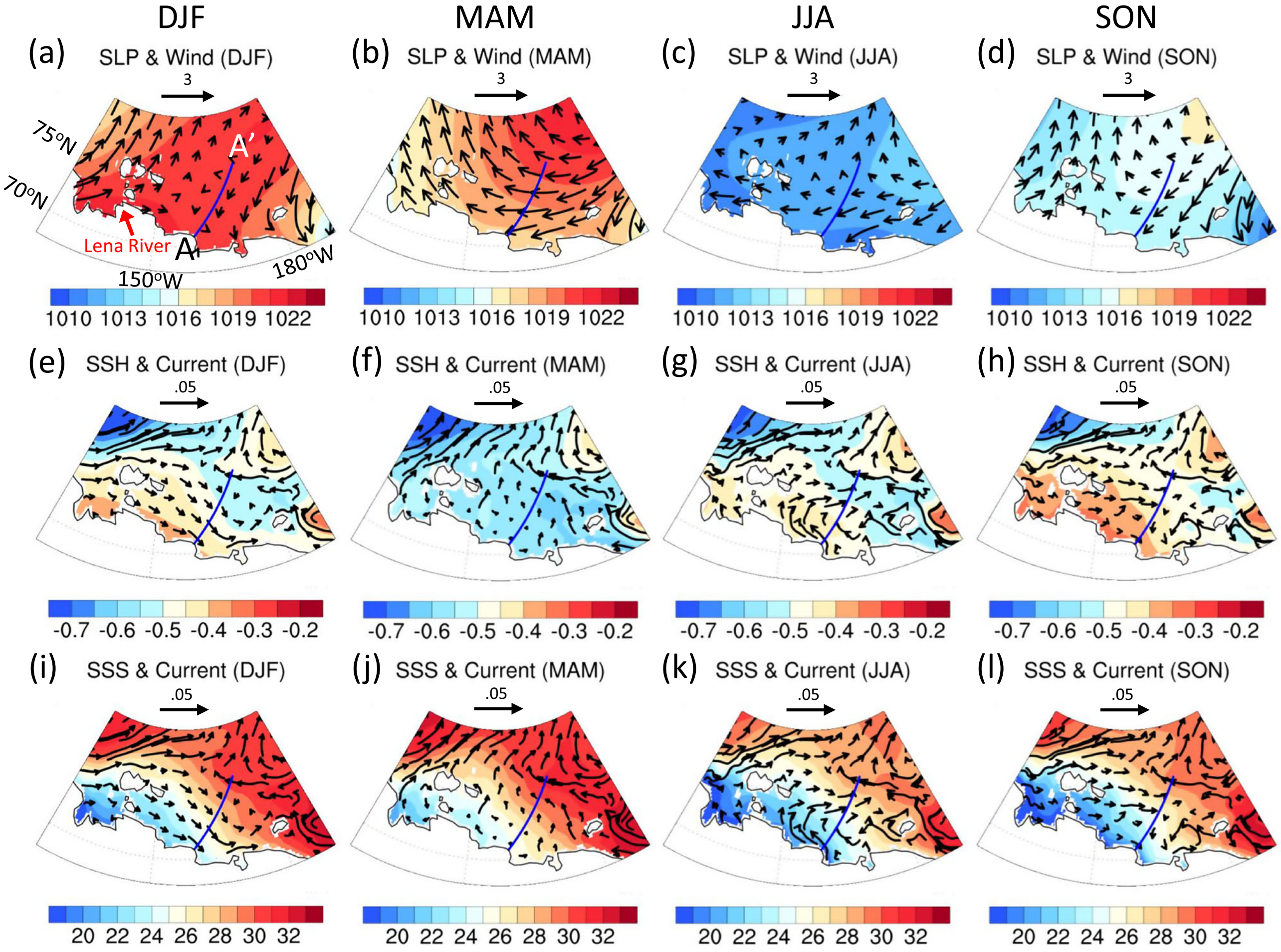

Fig. 2 | Seasonal atmospheric forcing and corresponding oceanic responses. **a**–**d** Seasonal mean sea-level pressure (SLP; colours, hPa) and 10-m wind vectors (arrows; m/s) from ERA5. **e**–**h** Sea surface height (SSH; colours, m) and surface current vectors (arrows; m/s) from ORAS5. (**i**–**l**) Sea surface salinity (SSS; colours; psu) and surface current vectors (arrows; m/s) from ORAS5. Transect A–A′ denotes the cross-shelf section analysed in Fig. 3.

gradient weakens and reverses, producing a westward current. These results confirm that the seasonal variability of the ESSC is fundamentally shaped by halosteric forcing, consistent with previous studies on the major contribution of freshwater input to SSH variability in the Siberian Shelf Seas[28].

Seasonal timeseries averaged along 73°N to 75°N (Fig. 4a) further clarify the role of salinity in modulating SSH variability in the East Siberian Sea. River discharge peaks in June, with approximately 83% of the annual runoff occurring between May and October. Coastal shelf salinity subsequently reaches a minimum in August, about two months after the peak runoff, and then increases during autumn and winter. The coastal shelf SSH follows this cycle, remaining highest in late summer and autumn when waters are freshest, and decreasing as salinity recovers. These timeseries suggest that freshwater input, combined with its delayed impact on salinity, contributes substantially to seasonal changes in SSH and the shelf current. Consistent with this interpretation, steric height decomposition showed that SSH variability in the ESSC region was dominated by the halosteric component, whereas the thermosteric contribution was negligible (Supplementary Fig. S3). To further evaluate the relative importance of different forcing mechanisms, we compared the geostrophic and wind-driven components of the shelf current (Fig. 4b). This analysis shows that the geostrophic component derived from SSH gradients dominates the seasonal cycle and closely matches the modelled total current, whereas the wind-driven Ekman component remains comparatively weak. These timeseries provide new evidence that the ESSC is primarily salinity-driven, with winds exerting only a secondary influence.

To assess whether large-scale winds modulate cross-shelf SSH gradients and the associated geostrophic flow, we examined the alongshore wind component and compared it with the cross-shelf SSH gradient (Fig. 4c, e). During April–May, predominantly easterly winds likely enhance freshwater release from the shelf, thereby weakening the cross-shelf SSH gradient and eastward geostrophic flow and permitting weak westward transport. Outside the spring transition, alongshore winds weaken substantially; however, the meridional SSH gradient continues to strengthen in step with the halosteric component. This result indicates that halosteric effects dominate the seasonal SSH evolution, with Ekman transport driven by zonal winds providing secondary but potentially important modulation, particularly during spring. Previous studies have shown that the shelf can adjust to wind-driven SSH states within a few days[44], and that winds can dominate sea level and current variability at synoptic timescales (~1.5–11 days)[45]. This implies that short-term wind events may trigger setup and release processes, and temporarily enhance cross-shelf exchange, thereby modulating shelf currents. Future high-resolution ocean model experiments spanning sub-daily to seasonal timescales will help in quantifying this wind-driven modulation relative to long-term salinity-driven responses.

Beyond the broad shelf current, this study identifies the Siberian Coastal Current along 71.5°–72°N as a key feature of the East Siberian Sea (Fig. 3). This narrow, buoyancy-driven jet, with a width of ~50–60 km adjacent to the coast, has been described as part of the pan-Arctic Riverine Coastal Domain[14], and observational studies have characterised the Siberian Coastal Current as a wind- and buoyancy-

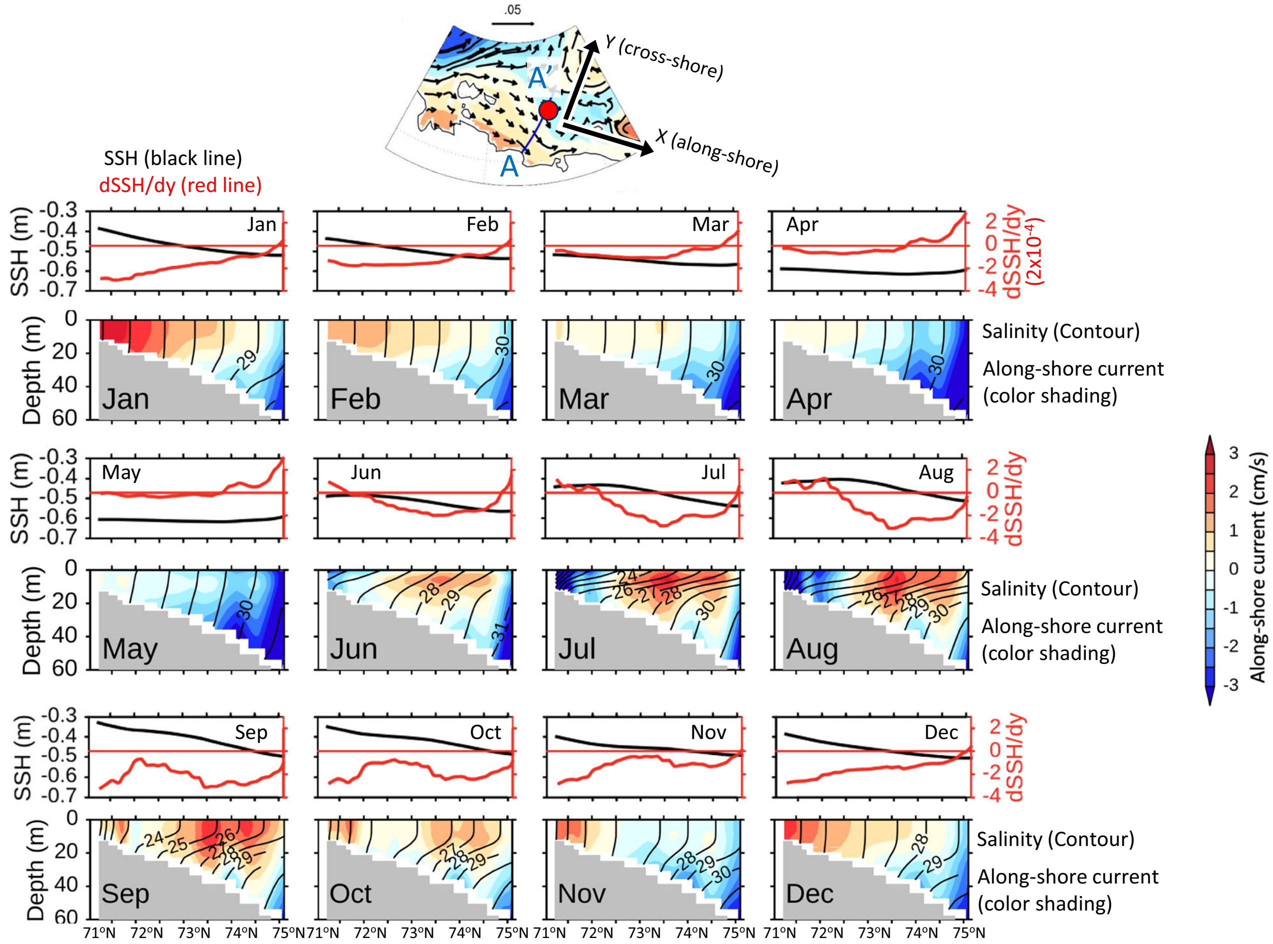

Fig. 3 | Seasonal evolution of ocean properties along the cross-shelf section A–A′. (Upper panels) SSH (black; ORAS5) and the cross-shore SSH gradient (red). (Lower panels) Salinity (contours) and along-shore velocity (colours; cm/s; eastward positive) from ORAS5.

forced coastal current along the East Siberian and Chukchi shelves[32,46,47]; however, its seasonal dynamics in the East Siberian Sea have not been clearly resolved. Here we show that early in summer (June and July), despite strong coastal freshening, persistent northeasterly winds maintain weakly positive SSH gradients (Fig. 2), thereby producing a temporary westward flow that opposes the prevailing current. However, by September, the winds subside, the salinity gradient steepens, and the flow returns eastward and persists throughout winter. This seasonal transition is illustrated in Fig. 4d, f. From September to April, the nearshore current follows a geostrophic balance associated with a negative offshore SSH gradient, whereas in summer, the SSH gradient weakens or reverses and winds become the dominant driver. These results demonstrate that, while winds can reverse the shelf current in summer, buoyancy forces promote an eastward, density-driven flow that is sustained throughout most of the year.

In summary, previous studies on the ESSC mainly described large-scale SSH and freshwater patterns, but did not resolve the detailed seasonal dynamics of the current. Seasonality has been attributed to wind and halocline forcing; however, the relative importance of these forcing mechanisms remains unclear. We addressed this issue by applying CSEOF to satellite and reanalysis SSH data, showing that the ESSC is primarily governed by a seasonal salinity cycle, while winds play only a secondary role. We also identified a narrow, buoyancy-driven Siberian Coastal Current (~50–60 km wide) that is observed, but not explicitly represented in the reanalysis products. By clarifying the mechanisms driving this variability, we provide new insights into a key but previously underrepresented feature of the Siberian shelf–current system.

Siberian Slope Current and SSH links to Arctic gateway transports

The second SSH mode (Mode 2) captures the boundary current along the Siberian slope at interannual timescales and is expressed as a basin–shelf dipole, with depressed SSH in the central Arctic Ocean and elevated SSH along the margins (Fig. 5a, b). The associated PC2 timeseries exhibited fluctuations with a period of approximately 2–3 year (Fig. 5c).

The atmospheric linkage of Mode 2 was broadly consistent with that reported in previous studies[41]. Using the AO index[34] and the AD index derived from sea-level pressure (SLP) patterns (Fig. S4), we found that the correlations between Mode 2 and atmospheric modes have shifted significantly over the past few decades (Fig. S5). During 1980–1994, PC2 was strongly correlated with the AO (r = 0.6–0.8), indicating AO-related forcing of this ocean mode. After 2000, this correlation weakened, and PC2 became more strongly aligned with the AD index, suggesting an increased influence of dipole-like pressure anomalies. The regression maps of SLP and winds (Fig. S6) confirmed this transition, with AO-related anomalies dominating from 1980 to 1994 and AD anomalies emerging from 2003 to 2017. These results are consistent with the "switchgear mechanism" proposed to modulate Atlantic inflow pathways[41]. Our analysis further shows that changes in the correlations between Mode 2 and atmospheric modes are embedded within a distinct SSH EOF mode that isolates the Siberian Slope Current, thereby reinforcing previous evidence for the role of the atmospheric transitions in Arctic Ocean circulation.

Moreover, we assessed how SSH modes relate to volume transports across major Arctic gateways. Positive SSH PC1 phases, characterised by

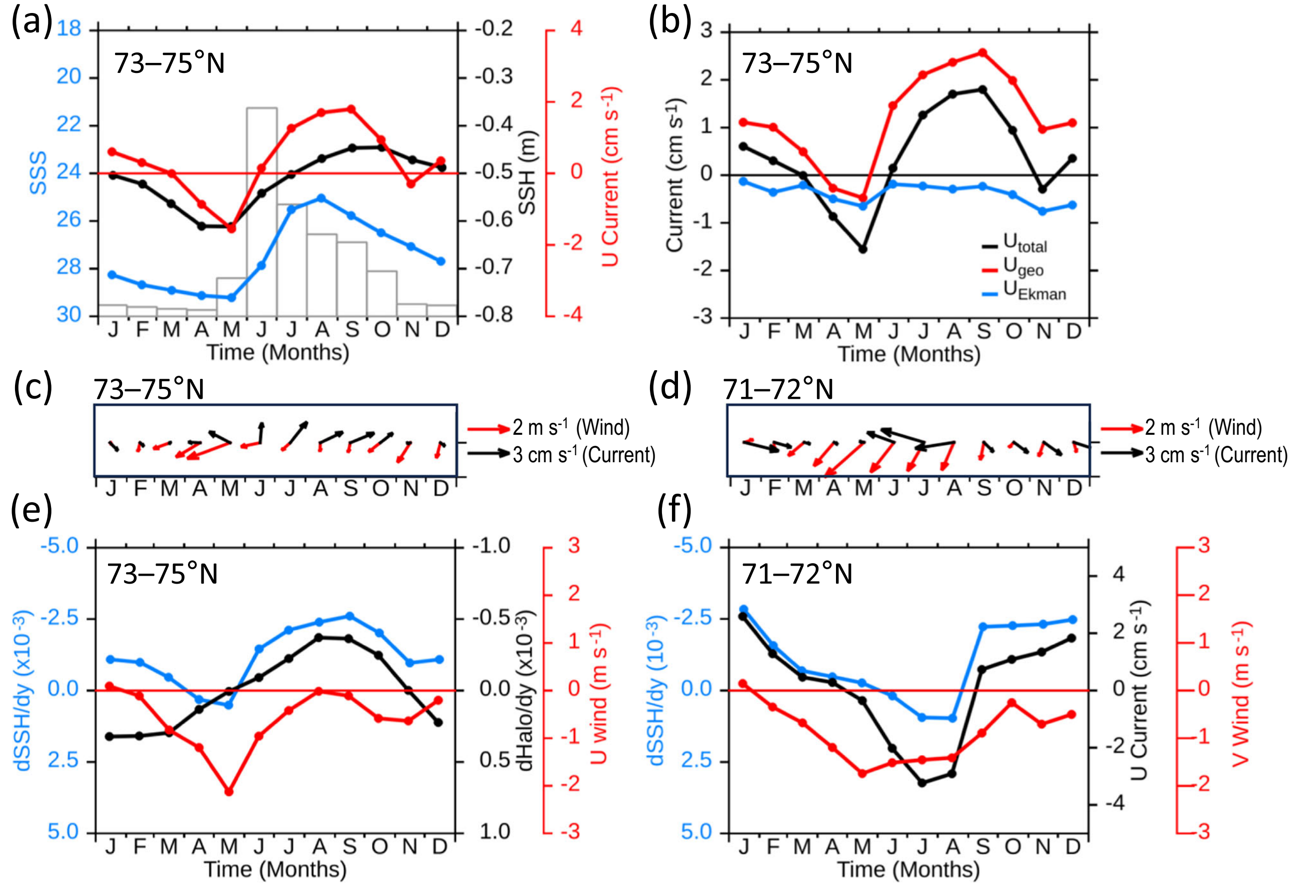

Fig. 4 | Seasonal cycles of the Eastern Siberian Shelf Current. **a** Seasonal variations of sea surface salinity (SSS; blue; axis inverted), sea surface height (SSH; black), and along-shore surface current velocity (red) from ORAS5, averaged along 73–75°N across section A–A′ (Fig. 3). Grey bars indicate Lena River discharge (0–0.1 Sv). **b** Along-shore surface current decomposed into geostrophic (U_{geo}; red) and wind-driven Ekman (U_{Ekman}; blue) components, with the total current shown in black, averaged along 73–75°N. **c**, **d** Monthly mean wind vectors (black arrows) and surface current vectors (red arrows) Eastern Siberian Shelf Current and the Siberian Coastal Current, respectively. **e** Seasonal variations of the cross-shelf SSH gradient (dSSH/dy; blue; axis inverted), the halosteric SSH gradient (dHalo/dy; black; axis inverted), and the along-shore wind component (red), averaged along 73–75°N. **f** Seasonal variability of the Siberian Coastal Current, illustrated by the cross-shore SSH gradient (dSSH/dy; blue; axis inverted), along-shore surface current (black), and cross-shore wind component (red), averaged along 71–72°N.

elevated coastal SSH along the East Siberian shelf, are associated with weaker Pacific inflow through the Bering Strait ($r = -0.39$, $p < 0.05$) and stronger Atlantic inflow through the Barents Sea Opening ($r = 0.48$, $p < 0.05$) (Fig. 6a, d). Consistent with these relationships, regression maps indicate reduced cross-strait pressure gradients during weak northward Bering inflow (Fig. 6b, c) and enhanced zonal SSH gradients along the Norwegian coast during strong Barents inflow (Fig. 6e, f), supporting the interpretation that PC1 is linked to gateway transports via SSH-gradient changes. In contrast, Fram Strait transport is more closely tied to Mode 2. Positive PC2 phases, characterised by lower basin SSH and higher shelf SSH, were associated with intensified cyclonic circulation and enhanced Atlantic inflow via the eastern Fram Strait (West Spitsbergen Current) ($r = 0.62$, $p < 0.05$; Fig. 6h, i). These results indicate that PC1 and PC2 capture distinct SSH-gradient configurations closely linked to Pacific and Atlantic exchanges across Arctic gateways.

In this study, volume transport through the straits was derived from ORAS5 and therefore requires further validation using observational data. This is especially critical for the Bering Strait, where even high-resolution models struggle to reproduce observed fluxes[21]. ORAS5 failed to reproduce the observed long-term increase in transport (Fig. S7a). However, after detrending, transport variability closely aligned with the observations (Fig. S7b), which is likely due to the assimilation of transport data after the 2000s. The regression patterns based on detrended ORAS5 transport agreed well with in situ measurements (Fig. S7c, d), supporting the robustness of our results when focusing on variability rather than long-term trends.

Wind mode driving Bering Strait transport variability

We investigated the wind mode driving Bering Strait transport variability using observational and reanalysis data. Observed transport data from mooring records[20] revealed a pronounced seasonal cycle and strong interannual variability (Fig. S8). Seasonal transport variability has been linked to wind forcing through SSH variations in the East Siberian Sea and the associated easterly winds in summer, whereas winter variability is influenced more strongly by local winds in the strait[48]. Wind stress has also been shown to influence transport variability on short time scales (on the order of one month)[21]. Building on this framework, we conducted regression analyses of SLP and SSH against Bering Strait transport (Fig. S9). The monthly regression patterns of SLP (Fig. S9a) revealed alternating dipole-like anomalies over the Bering Sea and East Siberia during most of the year, indicating wind-driven modulation of the flow. The corresponding SSH regressions (Fig. S9b) highlighted changes in cross-strait sea-level gradients, thereby confirming the dynamic link between basin-scale forcing and transport variability. This suggests that Arctic internal SLP variability is more dominant during summer, whereas local winds dominate during the rest of the year, consistent with previous findings[48].

Additionally, we investigated Bering Strait transport variability by identifying the underlying atmospheric drivers. We applied cyclostationary EOF analysis to ERA5 SLP data, which captures basin-scale atmospheric variability. The results reveal a dominant SLP mode that explains the coherent seasonal evolution of anomalies (Fig. 7a) and is consistent with the multi-year seasonal cycle of the ERA5 SLP climatology (Fig. S10), thereby

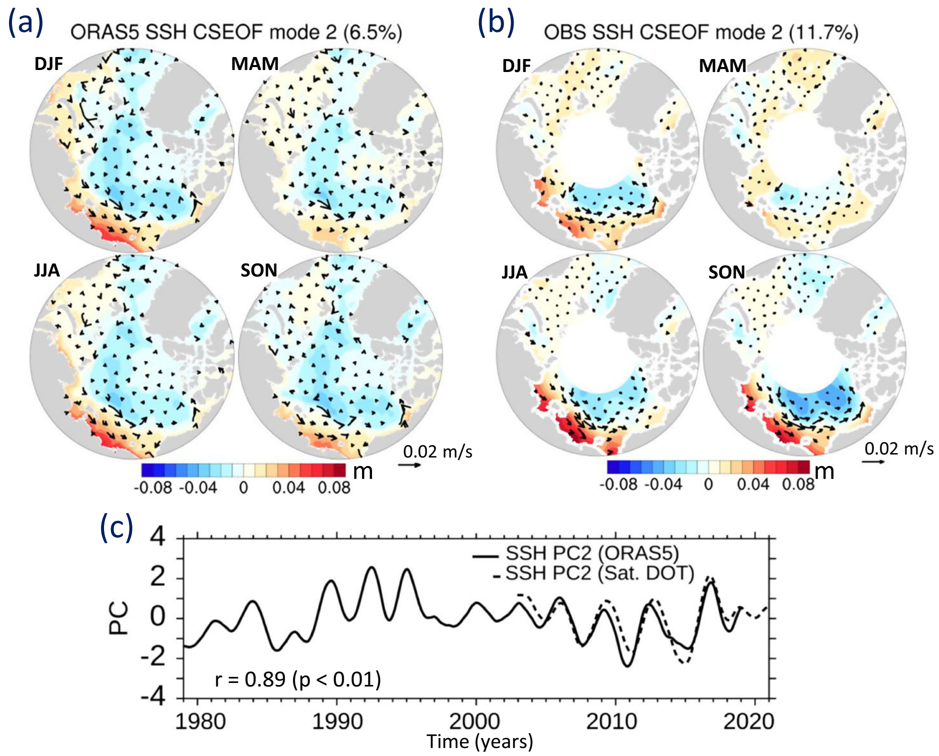

Fig. 5 | Interannual sea surface height (SSH) variability (Mode 2). **a** Spatial patterns of SSH anomalies (shading; m) and the associated geostrophic currents (vectors) for the second cyclostationary EOF (CSEOF) mode derived from ORAS5 reanalysis, shown for boreal winter (DJF), spring (MAM), summer (JJA), and autumn (SON). **b** Corresponding SSH anomaly patterns obtained from satellite-derived dynamic ocean topography (DOT). **c** Principal component (PC) timeseries of the interannual mode derived from ORAS5 (solid line) and satellite DOT (dashed line), showing strong agreement between the model and observations ($r = 0.89$, $p < 0.01$).

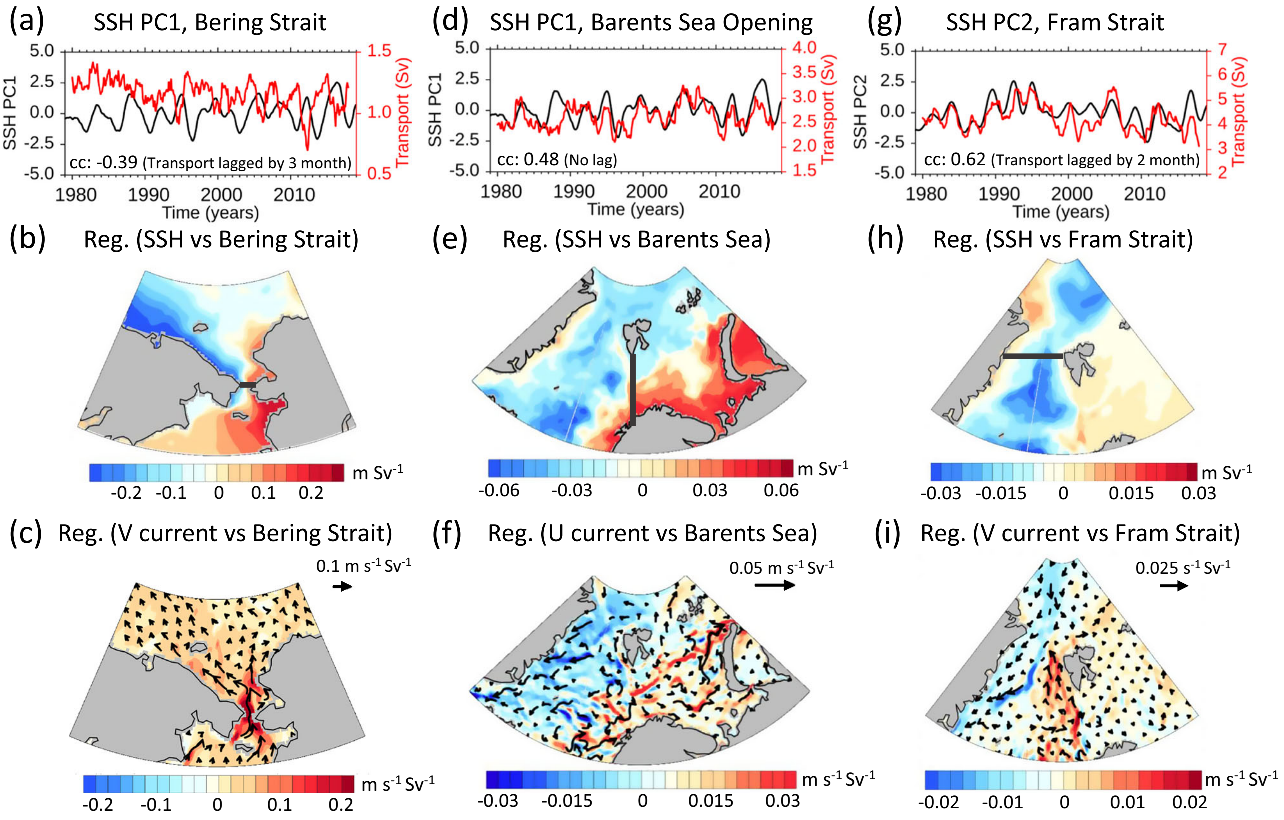

Fig. 6 | Relationships between SSH modes and Arctic gateway transports. **a**, **d**, **g** SSH principal components (PCs; black) derived from CSEOF compared with volume transport (red) through the Bering Strait (**a**), the Barents Sea Opening (**d**), and the Fram Starit (**g**). Correlation coefficients (cc), calculated after detrending the timeseries, are indicated. **b**, **e**, **h** Regression of SSH anomalies onto transport anomalies (units: m Sv^{-1}). **c**, **f**, **i** Regression of current anomalies (shading) and current vectors onto transport anomalies (units: m s^{-1} Sv^{-1}). Black lines denote the locations of transport sections.

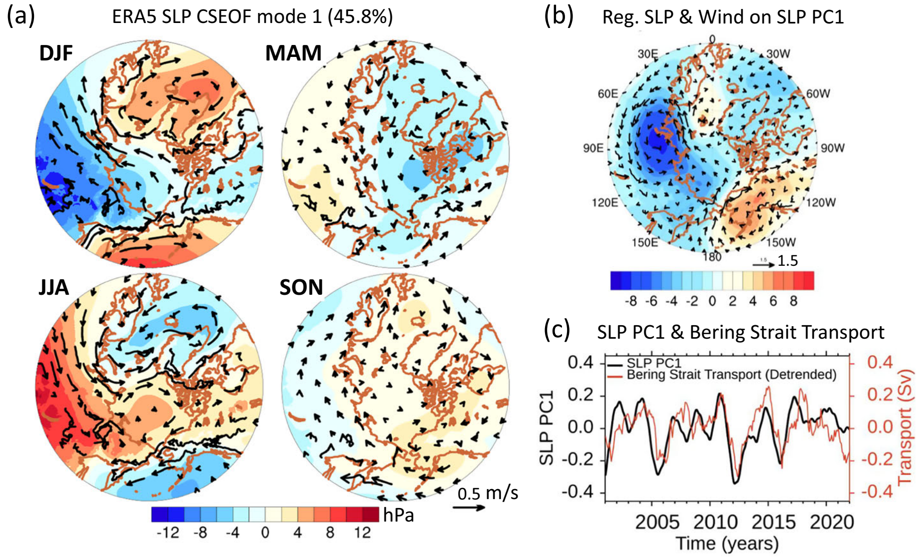

Fig. 7 | Dipole-like sea-level pressure mode regulating Bering Strait transport. **a** Seasonal evolution of the first cyclostationary EOF (CSEOF) mode of ERA5 sea level pressure (SLP; shading, hPa) and the associated geostrophic winds (vectors) over 50–90°N. **b** Regression of SLP and geostrophic winds onto SLP PC1 after applying a 13-month moving average to suppress the seasonal cycle. **c** Timeseries of SLP PC1 (black) and detrended observed Bering Strait volume transport derived from mooring observations (red; Woodgate, 2018) for the period 2001–2021.

supporting its physical relevance. Regression of the corresponding PC1 (Fig. 7b) onto the SLP and geostrophic wind fields highlights a dipole pressure pattern spanning Siberia and Alaska, placing the Bering Strait between opposing pressure centers. This configuration enhances along-strait winds through the resulting pressure gradient, thereby exerting basin-scale atmospheric control on Bering Strait transport variability.

In Figs. 7c and S11a, the associated PC1 timeseries (black) was strongly correlated with the observed Bering Strait transport variability (red) ($r = 0.70$, $p < 0.05$), peaking when PC1 led by approximately 3 months (Fig. S11b). This indicates that years with stronger SLP anomalies were associated with enhanced transport, highlighting that the dominant SLP mode explained nearly half of the observed transport variability. These results underscore the key role of large-scale atmospheric forcing in modulating Pacific Water inflow to the Arctic Ocean. Thus, the PC1 timeseries provides an index to anticipate changes in this inflow and the consequent impacts on Arctic Ocean circulation. By analogy with the switchgear mechanisms proposed for Arctic atlantification[41], this atmospheric control may represent a mechanism regulating Pacific Water inflow, commonly referred to as "pacificization".

Overall, our results demonstrate that SSH variability integrates buoyancy forcing, wind-driven circulation, and basin-scale atmospheric pressure patterns across both regional and gateway scales. This perspective establishes SSH as a physically grounded indicator of Arctic Ocean circulation and identifies the Siberian Arctic Ocean as a key region for improving understanding of future Arctic climate variability.

Methods

Reanalysis and satellite data

We used ocean reanalysis and satellite altimetry datasets to characterise Arctic SSH variability. The primary reanalysis dataset was ECMWF ORAS5 (Ocean ReAnalysis System 5)[49], spanning 1979–2018. ORAS5 assimilates a wide range of ocean observations and has been shown to perform well in simulating Arctic freshwater content[33]. For observational sea-level data, we used a merged dynamic ocean topography (DOT) record covering the period 2003–2020. This record combines the CPOM DOT dataset (2003–2014; derived from ICESat laser altimetry)[28] with CryoSat-2 radar altimetry data (2011–2020), following the approach described previously[50].

Atmospheric reanalysis data were used to interpret ocean variability. Sea level pressure (SLP) and surface wind fields were obtained from ERA5 data for the period 1979–2020[51]. The Arctic Oscillation (AO) index was defined as the principal component (PC) of the leading EOF of winter (DJF) SLP north of 20°N, following commonly used definition[34]. The Arctic Dipole (AD) index was defined as the PC of the second EOF mode of monthly SLP over the region 70–90°N (Fig. S4).

Observational datasets

Observed volume transport through the Bering Strait was obtained from the year-round mooring array maintained since the early 1990s[20,23]. For comparison with reanalysis products and CSEOF-based indices, we used monthly mean values. To isolate interannual variability, we removed linear trends and, where noted, applied a 13-month running mean. Positive transport was defined as northward flow into the Arctic Ocean.

To corroborate the seasonal cycle of the Eastern Siberian Shelf Current, we used in situ velocity measurements from the MB9 mooring on the Eastern Siberian Shelf[19]. The monthly-mean currents from MB9 were used to evaluate the timing and direction of the Eastern Siberian Shelf Current (Fig. S2), providing an independent observational constraint on the CSEOF-derived Mode 1 dynamics.

Cyclostationary empirical orthogonal function analysis

Empirical Orthogonal Function (EOF) analysis is a standard statistical technique used to identify dominant patterns of variability in geophysical datasets. To explicitly account for the periodic nature of the Arctic system, we applied the Cyclostationary EOF (CSEOF) method[42,52]. Unlike standard EOF analysis, CSEOF describes spatial patterns of monthly anomalies across the annual cycle, with the associated principal component timeseries representing year-to-year changes in the amplitude of the seasonal cycle. This approach has proven effective in studies of Arctic Ocean circulation and its climate linkages[43]. We conducted the CSEOF analysis after removing long-term trends and low-frequency variability longer than the interannual timescale from the SSH data. To suppress this long-term component, we detrended the records using a second-order polynomial fit. We applied the CSEOF method to the SSH fields and extracted the two leading modes, which were statistically well separated according to eigenvalue sampling uncertainty estimates[53] (Fig. S12). The principal component (PC) time series was normalized to unit standard deviation.

Regression and correlation analysis

Regression and correlation analyses were performed to examine the relationships among SLP, SSH, and surface currents with respect to the AO and AD indices. Regression analysis was used to identify how changes in ocean variables related to unit changes in the AO and AD timeseries, whereas correlation coefficients quantified the strength of the linear associations. All monthly time series were smoothed using a 13-month running mean to suppress seasonality[54]. Linear trends were removed from all timeseries to ensure stationarity.

To determine the correlation between SSH Mode 1 and Bering Strait transport, we applied the Hodrick–Prescott (HP) filter to capture the non-uniform long-term evolution of the transport record. The transport exhibited a sharp decline during the 1980s and the 1990s followed by a more gradual decrease. The HP filter separates nonlinear trend components from higher-frequency variability, allowing us to focus on the interannual signal of interest[55].

Steric, thermosteric, and halosteric height anomalies

The steric, thermosteric, and halosteric height anomalies were computed following established formulations[56].

$$\eta'_s = -\frac{1}{\rho_0}\int_{-H}^{0}(\rho(T,S,p) - \rho(\bar{T},\bar{S},p))dz \tag{1}$$

$$\eta'_{st} = -\frac{1}{\rho_0}\int_{-H}^{0}(\rho(T,\bar{S},p) - \rho(\bar{T},\bar{S},p))dz \tag{2}$$

$$\eta'_{ss} = -\frac{1}{\rho_0}\int_{-H}^{0}(\rho(\bar{T},S,p) - \rho(\bar{T},\bar{S},p))dz \tag{3}$$

where T (°C), S, and p (dbar) are potential temperature, salinity, and pressure, respectively; $\bar{T}$ and $\bar{S}$ denote the climatological mean temperature and salinity, respectively; ρ (kg m^{-3}) is seawater density, ρ_0 is the reference density (1025.0 kg m^{-3}), and H (m) is the local bottom depth.

Data availability

Altimetry-derived sea-surface-height products are available from the CPOM Dynamic Ocean Topography portal (http://www.cpom.ucl.ac.uk/dynamic_topography/) and PANGAEA (https://doi.org/10.1594/PANGAEA.931869). ORAS5 ocean reanalysis data are available from the Copernicus Climate Data Store (https://doi.org/10.24381/cds.67e8eeb7), and ERA5 atmospheric reanalysis data from the C3S Climate Data Store (https://cds.climate.copernicus.eu/datasets/reanalysis-era5-single-levels?tab=overview). Mooring data are available via the Arctic Data Center (https://arcticdata.io/catalog/view/doi:10.18739/A2Q23R23Z). Bering Strait volume transport estimates are available from the University of Washington APL archive (http://psc.apl.washington.edu/HLD/Bstrait/Data/BeringStraitMooringDataArchive.html).

Received: 10 October 2025; Accepted: 16 March 2026;
Published online: 01 April 2026

References

1. Rantanen, M. et al. The Arctic has warmed nearly four times faster than the globe since 1979. *Commun. Earth Environ.* **3**, 168 (2022).
2. Polyakov, I. V. et al. One more step toward a warmer Arctic. *Geophys. Res. Lett*. **32**, L17605 (2005).
3. Bekryaev, R. V., Polyakov, I. V. & Alexeev, V. A. Role of polar amplification in long-term surface air temperature variations and modern Arctic warming. *J. Clim.* **23**, 3888–3906 (2010).
4. Overland, J. et al. The urgency of Arctic change. *Polar Sci*. **21**, 6–13 (2019).
5. Sumata, H., Steur, L. de, Divine, D. V., Granskog, M. A. & Gerland, S. Regime shift in Arctic Ocean sea ice thickness. *Nature* **615**, 443–449 (2023).
6. Kwok, R. & Rothrock, D. A. Decline in Arctic sea ice thickness from submarine and ICESat records. *Geophys. Res. Lett.* **36**, 1958–2008 (2009).
7. Smedsrud, L. H., Halvorsen, M. H., Stroeve, J. C., Zhang, R. & Kloster, K. Fram Strait sea ice export variability and September Arctic sea ice extent over the last 80 years. *Cryosphere* **11**, 65–79 (2016).
8. Kim, Y.-H., Min, S.-K., Gillett, N. P., Notz, D. & Malinina, E. Observationally-constrained projections of an ice-free Arctic even under a low emission scenario. *Nat. Commun.* **14**, 3139 (2023).
9. Morison, J. et al. Changing Arctic Ocean freshwater pathways. *Nature* **481**, 66–70 (2012).
10. Rabe, B. et al. Arctic Ocean basin liquid freshwater storage trend 1992–2012. *Geophys. Res. Lett.* **41**, 961–968 (2014).
11. Serreze, M. C. & Barrett, A. P. Characteristics of the Beaufort Sea High. *J. Clim.* **24**, 159–182 (2011).
12. Morison, J. et al. The cyclonic mode of Arctic Ocean circulation. *J. Phys. Oceanogr.* **51**, 1053–1075 (2021).
13. Wilson, C. et al. Significant variability of structure and predictability of Arctic Ocean surface pathways affects basin-wide connectivity. *Commun. Earth Environ.* **2**, 164 (2021).
14. Carmack, E., Winsor, P. & Williams, W. The contiguous panarctic Riverine Coastal Domain: A unifying concept. *Prog. Oceanogr.* **139**, 13–23 (2015).
15. Osadchiev, A. A., Pisareva, M. N., Spivak, E. A., Shchuka, S. A. & Semiletov, I. P. Freshwater transport between the Kara, Laptev, and East-Siberian seas. *Sci. Rep.* **10**, 13041 (2020).
16. Jung, J., Lee, Y., Cho, K., Yang, E. J. & Kang, S. Spatial distributions of riverine and marine dissolved organic carbon in the western arctic ocean: results from the 2018 Korean expedition. *J. Geophys. Res.: Oceans* **127**, e2021JC017718 (2022).
17. Nishino, S. et al. Atlantic-origin water extension into the Pacific Arctic induced an anomalous biogeochemical event. *Nat. Commun.* **14**, 6235 (2023).
18. Polyakov, I. V. et al. Greater role for Atlantic inflows on sea-ice loss in the Eurasian Basin of the Arctic Ocean. *Science* **356**, 285–291 (2017).
19. Polyakov, I. V. et al. Role of sea ice, stratification, and near-inertial oscillations in shaping the upper Siberian Arctic Ocean currents. *Ocean Sci.* **21**, 3105–3122 (2025).
20. Woodgate, R. A. Increases in the Pacific inflow to the Arctic from 1990 to 2015, and insights into seasonal trends and driving mechanisms from year-round Bering Strait mooring data. *Prog. Oceanogr.* **160**, 124–154 (2018).
21. Nguyen, A. T., Woodgate, R. A. & Heimbach, P. Elucidating large-scale atmospheric controls on Bering Strait throughflow variability using a data-constrained ocean model and its adjoint. *J. Geophys. Res.: Oceans* **125**, e2020JC016213 (2020).
22. Zhang, W., Wang, Q., Wang, X. & Danilov, S. Mechanisms driving the interannual variability of the Bering Strait throughflow. *J. Geophys. Res.: Oceans* **125**, e2019JC015308 (2020).
23. Woodgate, R. A. & Peralta-Ferriz, C. Warming and freshening of the Pacific inflow to the Arctic from 1990-2019 implying dramatic shoaling in Pacific winter water ventilation of the Arctic water column. *Geophys. Res. Lett*. **48**, e2021GL092528 (2021).
24. Pickart, R. S. et al. The Pacific water flow branches in the eastern Chukchi Sea. *Prog. Oceanogr.* **219**, 103169 (2023).
25. Proshutinsky, A. et al. Secular sea level change in the Russian sector of the Arctic Ocean. *J. Geophys. Res. Oceans* **109**, C03042 (2004).
26. Proshutinsky, A. et al. Beaufort Gyre freshwater reservoir: State and variability from observations. *J. Geophys. Res. Oceans* **114**, C00A10 (2009).
27. Giles, K. A., Laxon, S. W., Ridout, A. L., Wingham, D. J. & Bacon, S. Western Arctic Ocean freshwater storage increased by wind-driven spin-up of the Beaufort Gyre. *Nat. Geosci.* **5**, 194–197 (2012).
28. Armitage, T. W. K. et al. Arctic sea surface height variability and change from satellite radar altimetry and GRACE, 2003–2014. *J. Geophys. Res. Oceans* **121**, 4303–4322 (2016).
29. Serreze, M. C. et al. The large-scale freshwater cycle of the Arctic. *J. Geophys. Res. Oceans* **111**, C11010 (2006).
30. Yamamoto-Kawai, M. et al. Surface freshening of the Canada Basin, 2003–2007: River runoff versus sea ice meltwater. *J. Geophys. Res. Oceans* **114**, C00A05 (2009).

31. Proshutinsky, A. Y. & Johnson, M. A. Two circulation regimes of the wind-driven Arctic Ocean. *J. Geophys. Res.: Oceans* **102**, 12493–12514 (1997).
32. Weingartner, T. J. et al. The Siberian Coastal Current: A wind- and buoyancy-forced Arctic coastal current. *J. Geophys. Res.: Oceans* **104**, 29697–29713 (1999).
33. Hall, S. B., Subrahmanyam, B. & Morison, J. H. Intercomparison of salinity products in the Beaufort Gyre and Arctic Ocean. *Remote Sens* **14**, 71 (2021).
34. Thompson, D. W. J. & Wallace, J. M. The Arctic Oscillation signature in the wintertime geopotential height and temperature fields. *Geophys. Res. Lett.* **25**, 1297–1300 (1998).
35. Wu, B., Wang, J. & Walsh, J. E. Dipole anomaly in the winter Arctic atmosphere and its association with sea ice motion. *J. Clim.* **19**, 210–225 (2006).
36. Overland, J. E. & Wang, M. Large-scale atmospheric circulation changes are associated with the recent loss of Arctic sea ice. *Tellus A* **62**, 1–9 (2010).
37. Peralta-Ferriz, C., Morison, J. H., Wallace, J. M., Bonin, J. A. & Zhang, J. Arctic ocean circulation patterns revealed by GRACE. *J. Clim.* **27**, 1445–1468 (2014).
38. Armitage, T. W. K., Bacon, S. & Kwok, R. Arctic sea level and surface circulation response to the Arctic Oscillation. *Geophys. Res. Lett.* **45**, 6576–6584 (2018).
39. Wang, Q. et al. A Review of Arctic–subarctic ocean linkages: past changes, mechanisms, and future projections. *Ocean-Land-Atmos. Res*. **2**, 0013 (2023).
40. Henry, O. et al. Tide gauge-based sea level variations since 1950 along the Norwegian and Russian coasts of the Arctic Ocean: Contribution of the steric and mass components. *J. Geophys. Res. Oceans* **117**, n/a-n/a (2012).
41. Polyakov, I. V. et al. Fluctuating Atlantic inflows modulate Arctic atlantification. *Science* **381**, 972–979 (2023).
42. Kim, K.-Y. & North, G. R. EOFs of harmonizable cyclostationary processes. *J. Atmos. Sci.* **54**, 2416–2427 (1997).
43. Kim, K.-Y., Hamlington, B. D., Na, H. & Kim, J. Mechanism of seasonal Arctic sea ice evolution and Arctic amplification. *Cryosphere* **10**, 2191–2202 (2016).
44. Winsor, P. & Chapman, D. C. Pathways of Pacific water across the Chukchi Sea: A numerical model study. *J. Geophys. Res.: Oceans* **109**, (2004).
45. Danielson, S. L. et al. Oceanic routing of wind-sourced energy along the Arctic continental shelves. *Front. Mar. Sci.* **7**, 509 (2020).
46. Münchow, A., Weingartner, T. J. & Cooper, L. W. The summer hydrography and surface circulation of the East Siberian Shelf Sea. *J. Phys. Oceanogr.* **29**, 2167–2182 (1999).
47. Wang, X. et al. Distribution and transport of water masses in the East Siberian Sea and their impacts on the Arctic halocline. *J. Geophys. Res.: Oceans* **126**, e2020JC016523 (2021).
48. Peralta-Ferriz, C. & Woodgate, R. A. The dominant role of the East Siberian Sea in driving the oceanic flow through the Bering Strait—conclusions from GRACE ocean mass satellite data and in situ mooring observations between 2002 and 2016. *Geophys. Res. Lett.* **44**, 11,472–11,481 (2017).
49. Zuo, H., Balmaseda, M. A., Tietsche, S., Mogensen, K. & Mayer, M. The ECMWF operational ensemble reanalysis–analysis system for ocean and sea ice: a description of the system and assessment. *Ocean Sci.* **15**, 779–808 (2019).
50. Doglioni, F. et al. Sea surface height anomaly and geostrophic current velocity from altimetry measurements over the Arctic Ocean (2011–2020). *Earth Syst. Sci. Data Discuss.* **2022**, 1–51 (2022).
51. Hersbach, H. et al. The ERA5 global reanalysis. *Q. J. R. Meteorol. Soc.* **146**, 1999–2049 (2020).
52. Kim, K.-Y., Hamlington, B. & Na, H. Theoretical foundation of cyclostationary EOF analysis for geophysical and climatic variables: Concepts and examples. *Earth-Sci. Rev.* **150**, 201–218 (2015).
53. North, G. R., Bell, T. L., Cahalan, R. F. & Moeng, F. J. Sampling errors in the estimation of empirical orthogonal functions. *Mon. Weather Rev.* **110**, 699–706 (1982).
54. Mudelsee, M. Trend analysis of climate time series: A review of methods. *Earth-Sci. Rev.* **190**, 310–322 (2019).
55. Domala, V. & Kim, T. Application of Empirical Mode Decomposition and Hodrick Prescot filter for the prediction single step and multistep significant wave height with LSTM. *Ocean Eng* **285**, 115229 (2023).
56. Yashayaev, I. & Zhang, Y. Concurrent warming, freshening and cessation of deep convection in the Labrador Sea raised its sea level to a record high. *Nat. Commun.* **16**, 10721 (2025).

Acknowledgements

We gratefully acknowledge Prof. Kwang-Yul Kim for developing the cyclostationary EOF methodology and for providing the associated analysis code. This research was supported by Korea Institute of Marine Science & Technology Promotion (KIMST) grant funded by the Ministry of Oceans and Fisheries (KIMST RS-2021-KS211500, Korea-Arctic Ocean Warming and Response of Ecosystem, KOPRI).

Author contributions

T.P. conceived the study, performed the analyses, and drafted the manuscript. K.H.C. contributed to data analysis and scientific discussions. E.L. processed and curated the datasets. I.V.P. provided key observational datasets and contributed substantial scientific input and comments. E.J.Y. contributed to the study objectives and overall project coordination. All authors contributed to discussions and manuscript preparation.

Competing interests

The authors declare no competing interests.

Additional information

Supplementary information The online version contains supplementary material available at https://doi.org/10.1038/s41612-026-01393-w.

Correspondence and requests for materials should be addressed to Taewook Park.